Quantum oscillations in a bilayer with broken mirror symmetry: A minimal model for YBa_{2}Cu_{3}O_{6+δ}

Akash V. Maharaj, Yi Zhang, B. J. Ramshaw, and S. A. Kivelson

Phys. Rev. B **93**, 094503 — Published 1 March 2016

DOI: 10.1103/PhysRevB.93.094503

Quantum oscillations in a bilayer with broken mirror symmetry: a minimal model for $YBa_2Cu_3O_{6+\delta}$

Akash V. Maharaj[1], Yi Zhang[1], B.J. Ramshaw[2], and S. A. Kivelson[1]
[1] *Department of Physics, Stanford University, Stanford, California 94305, USA. and*
[2] *Los Alamos National Laboratory, Los Alamos, New Mexico 87545, USA.*
(Dated: February 16, 2016)

Using an exact numerical solution and semiclassical analysis, we investigate quantum oscillations (QOs) in a model of a bilayer system with an anisotropic (elliptical) electron pocket in each plane. Key features of QO experiments in the high temperature superconducting cuprate YBCO can be reproduced by such a model, in particular the pattern of oscillation frequencies (which reflect "magnetic breakdown" between the two pockets) and the polar and azimuthal angular dependence of the oscillation amplitudes. However, the requisite magnetic breakdown is possible only under the assumption that the horizontal mirror plane symmetry is spontaneously broken and that the bilayer tunneling, $t_\perp$, is substantially renormalized from its 'bare' value. Under the assumption that $t_\perp = \tilde{Z} t_\perp^{(0)}$, where $\tilde{Z}$ is a measure of the quasiparticle weight, this suggests that $\tilde{Z} \lesssim 1/20$. Detailed comparisons with new $YBa_2Cu_3O_{6.58}$ QO data, taken over a very broad range of magnetic field, confirm specific predictions made by the breakdown scenario.

Quantum oscillations (QOs) are a spectacular consequence of the presence of a Fermi surface. Their observation in the high T_c cuprate superconductors[1–15] combined with recent observations of charge density wave correlations[16–31], have led to a compelling view of the non-superconducting "normal" state of the underdoped cuprates at high fields, $H > H_c$, and low temperatures, $T \ll T_c$. In this regime, small electron-like Fermi pockets arise from reconstruction of a larger hole-like Fermi surface presumably due to translation symmetry breaking in the form of bidirectional[64] charge-density-wave (CDW) order[32–43].

However, to date, no theory of Fermi-surface reconstruction by a simple CDW can simultaneously account for the Fermi pockets and the relatively small magnitude of the measured specific heat,[44,45] which presumably reflects the persistence a pseudo-gap that removes other portions of the original (large) Fermi surface.[65] Thus, rather than trying to infer the *origin* of the Fermi pockets, we explore a generic model of a single bilayer split pocket to elucidate general features that can most easily *account for* the salient features of the QOs.

Specifically, we focus on the bilayer cuprate YBCO, in which quantum oscillations have been studied in greatest detail. The frequency of the QOs and the negative values of various relevant transport coefficients[2] establish the existence of an electron pocket enclosing an area of order 2% of the Brillouin zone. A typical spectrum of QOs in underdoped YBCO is shown in Fig. 1. While there is some suggestive evidence of more than one basic frequency—which might suggest more than one pocket per plane[38,46,47]—we instead adopt and further elucidate a suggestion of Harrison and Sebastian[10,34,36] that the "three-peak" structure of the spectrum of oscillation frequencies reflects magnetic breakdown orbits associated with a single, bilayer-split pocket. In refining this suggestion, we show that, although many aspects of the QO experiments can be successfully accounted for in this way, the requisite magnetic breakdown is forbidden in the presence of a mirror symmetry that exchanges the planes of the bilayer; thus, a heretofore unnoticed implication is that the high field phase must spontaneously break this symmetry. Other striking features of the quantum oscillations are the existence of prominent "spin zeros"[9] and a strong C_4 symmetric dependence of the oscillation amplitudes on the in-plane component of the magnetic field with no evidence of the enhancement at the "Yamaji angle" expected from the simplest "neck and belly" structure of a quasi-2D Fermi surface[13].[66]

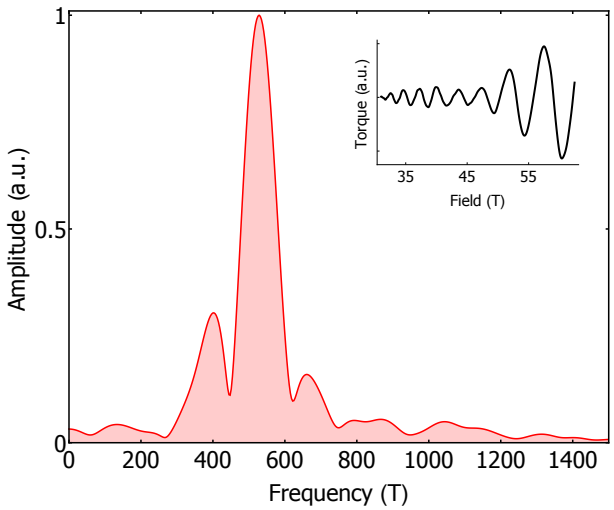

FIG. 1: Typical Fourier transform of QOs of the magnetic torque for underdoped $YBa_2Cu_3O_{6.58}$ ($T_c = 60$ K, $p \approx 11\%$) showing the characteristic symmetrically split "three peak" structure. Raw torque data is shown in the inset, taken at $T \approx 1.5$K, for a field range of 31 to 62.6 T. Structure above 700 T in the Fourier transform is harmonic content.

We show that all these experimental features are consistent with a simple model in which there is an elliptical Fermi pocket in each of the planes of a bilayer, with

their principal axes rotated by $\pi/2$ relative to each other. In terms of broken symmetries, this is consistent with a "criss-crossed-nematic" *component* of whatever ordered state exists in this range of T and B. We assume a $\vec{k}$ independent coupling between the layers within a bilayer, $t_\perp$, and we neglect all inter-bilayer coupling, $t'_\perp \approx 0$. As we will discuss in Sec. IV, both these assumptions seem more natural in the context of experiments and band-structure calculations of YBCO than those made by Sebastian *et al.* in their pioneering treatment of this same problem. Specifically, Sebastian *et al.*[10,34,36] assumed a strong $\vec{k}$ dependence associated with a presumed vanishing of $t_\perp$ in certain crystallographic directions, the significant role of non-zero $t'_\perp$, and broken translation symmetry in the c-direction[67]; these do not feature in our minimal model.

Finally, we have uncovered a quantitative issue with potential qualitative implications for magnetic breakdown. The magnitude of $t_\perp$ sets the size of the gap between bilayer split Fermi surfaces thus controlling the importance of magnetic breakdown orbits. Because our numerical approach treats magnetic breakdown exactly (rather than using a Zenner tunneling approach), we are uniquely placed to examine this effect. We have found that in order for magnetic breakdown to play a significant role in the relevant range of B, it is necessary to assume that $t_\perp$ is 20 times or more smaller than its "bare" value $t_\perp^{(0)}$, which can be estimated either from band-structure calculations[48–50] or from angle resolved photoemission (ARPES) studies of overdoped YBCO.[51] As was emphasized both in ARPES measurements[51] and previous theoretical studies[50,52–54], the ratio $\tilde{Z} \equiv t_\perp/t_\perp^{(0)}$ is a measure of the degree of single particle interlayer coherence, and so is related[68] to the quasiparticle weight. This implies that the quasiparticles responsible for the QOs are very strongly renormalized, with $\tilde{Z} \lesssim 0.05$, which in turn suggests that they are likely to be rather subtle, emergent features of the high field, low temperature state. One should be cautious in interpreting higher energy or temperature phenomena in terms of a Fermi liquid of these excitations.

Logic and Organization of the Paper

In Sec. I, we define an explicit lattice model of non-interacting electrons with a band-structure engineered to produce the desired small elliptical electron-like Fermi pockets (shown in Fig. 2), and describe the numerical algorithm we have used to obtain exact results for this model as a function of an applied magnetic field. To orient ourselves, in Sec. II we sketch the semiclassical analysis (including the effects of magnetic breakdown) which will allow us to associate the oscillation frequencies we will encounter with the geometry of the Fermi surface. We then present results of the numerical analysis of the model in Sec. III: In Fig. 3 we present the ideal QO spectrum, while in Fig. 4 we exhibit the way in which higher harmonics are rapidly suppressed by a non-infinite quasi-particle lifetime. We then present spectra that result when the range of magnetic fields analyzed is confined to realistically accessible values, discussing both qualitative and quantitative trends as parameters are tuned (see Fig. 5). We also study the polar and azimuthal angular dependence of the QOs (see Fig. 6 and 7), and develop accurate semiclassical arguments to interpret our numerical results (see Figs. 7 and 8). Finally, in Sec. IV we discuss the implications of our results for the interpretation of experiments in the cuprates, including comparison with newly presented QO data taken on $YBa_2Cu_3O_{6.58}$, which is used to test key features of the magnetic breakdown scenario discussed here. We also discuss the connection with other related theoretical work.

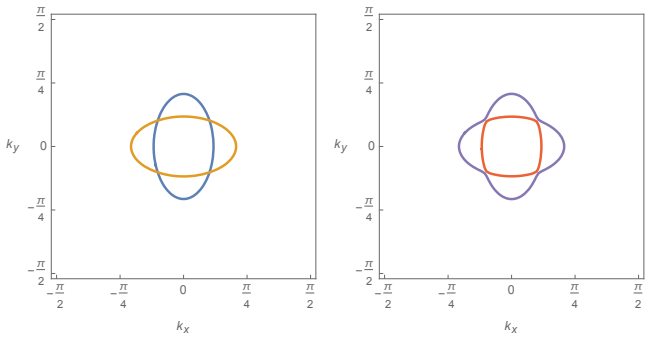

(a) $t_\perp = 0$ (b) $t_\perp = 0.005 t_a$

FIG. 2: The Fermi surface of the bilayer system in (a) the absence ($t_\perp = 0$) and (b) the presence ($t_\perp = 0.005 t_a$) of an isotropic interlayer tunneling $t_\perp$. The parameters used are $t_b = t_a/3$ and $\mu = -2.5306 t_a$. Note that we have zoomed in to an area that is one quarter of the full (unreconstructed) Brillouin zone.

I. THE MODEL

We study a tight-binding model of electrons hopping on two coupled layers, each consisting of a square lattice with purely nearest-neighbor hopping elements. In the presence of an arbitrarily oriented magnetic field the Hamiltonian of this model has the form

$$\begin{aligned} H = & \sum_{\langle \vec{r}_i, \vec{r}_j \rangle; \sigma} \sum_{\lambda} -t_{\vec{r}_i - \vec{r}_j; \lambda} \left(e^{i\Phi_{ij}} c^\dagger_{\vec{r}_i,\lambda,\sigma} c_{\vec{r}_j,\lambda,\sigma} + \text{H.c.} \right) \\ & + \sum_{\vec{r}_i;\sigma} \sum_{\lambda} 4\pi \tilde{g} B \sigma c^\dagger_{\vec{r}_i,\lambda,\sigma} c_{\vec{r}_i,\lambda,\sigma} \\ & - \sum_{\vec{r}_i;\sigma} t_\perp \left(e^{i\Phi^z_i} c^\dagger_{\vec{r}_i,1,\sigma} c_{\vec{r}_i,2,\sigma} + \text{H.c.} \right) \end{aligned} \tag{1}$$

where $c^\dagger_{\vec{r}_i,\lambda,\sigma}$ is an electron creation operator at position $\vec{r}_i$ in layer $\lambda = 1, 2$ with spin $\sigma = \pm 1/2$, and $t_{\vec{r}_i - \vec{r}_j;\lambda}$ denotes the appropriate hopping matrix element in layer λ, while $t_\perp$ is the (isotropic) hopping between each layer in

the bilayer and $\tilde{g}$ controls the strength of Zeeman splitting. Here, $\Phi_{ij} = \int_{\vec{r}_j}^{\vec{r}_i} \boldsymbol{A}(\boldsymbol{r}) d\boldsymbol{r}$ is the phase obtained by an electron hopping from site $\vec{r}_j$ to $\vec{r}_i$ in units in which $\hbar c/e = 1$, while $\Phi_i^{\tilde{z}}$ is the phase obtained upon tunneling from one layer to the next at position $\vec{r}_i$. To obtain perpendicularly oriented elliptical pockets we set $t_{\hat{x};1} = t_{\hat{y};2} = t_a$, and $t_{\hat{y};1} = t_{\hat{x};2} = t_b$. In the absence of a magnetic field this Hamiltonian can be diagonalized to give the spectrum $E_\pm(\boldsymbol{k})$ where $\boldsymbol{k} = (k_x, k_y)$ is a two dimensional Bloch wavevector, with

$$E_\pm(\boldsymbol{k}) = \varepsilon_+(\boldsymbol{k}) \pm \sqrt{\varepsilon_-^2(\boldsymbol{k}) + t_\perp^2} \tag{2}$$

$$\varepsilon_\pm(\boldsymbol{k}) = -(t_a \pm t_b)\cos(k_x) - (t_b \pm t_a)\cos k_y. \tag{3}$$

The Fermi surface with and without interlayer tunneling, with the choice of $t_b = t_a/3$ and a chemical potential of $\mu = -2.5306 t_a$ is shown in Fig. 2.

In the absence of $t_\perp$, the addition of a magnetic field maps Eq.1 to two copies of the Hofstadter problem. Upon coupling the layers, and for fields at arbitrary polar (θ) and selected azimuthal angles (ϕ), we can always pick a gauge that preserves translation symmetry along the in-plane direction of the magnetic field, $\hat{e}$. This allows us to take the Fourier transform along $\hat{e}$, and map Eq. 1 to a modified Harper's equation. For simplicity, we will consider the case in which the magnetic field lies in the $y-z$ plane, with the generalization to arbitrary orientation deferred to Appendix A. With $\boldsymbol{B} = B\,(0, \sin\theta, \cos\theta)$, we can choose the gauge

$$\boldsymbol{A} = (0, 2\pi\Phi x, -2\pi\Phi x \tan\theta)\,, \tag{4}$$

where $\Phi = B\cos\theta$ is the density of magnetic flux quanta per $x-y$ lattice plaquette (in units in which the plaquette area is 1).

Upon Fourier transforming the Hamiltonian in the $\hat{y}$ direction we have $H = \sum_{k_y,\sigma} \hat{H}_{k_y,\sigma}$:

$$\begin{aligned}\hat{H}_{k_y,\sigma} = &\sum_{x,\lambda} \Big\{ t_{\hat{x},\lambda} \left(c^\dagger_{(x+1,k_y);\lambda;\sigma} + c^\dagger_{(x-1,k_y);\lambda;\sigma} \right) \\ &+ \left[2t_{\hat{y},\lambda} \cos\left(2\pi\Phi x - k_y\right) + \frac{4\pi\tilde{g}\Phi\sigma}{\cos\theta} \right] c^\dagger_{(x,k_y);\lambda;\sigma} \Big\} c_{(x,k_y);\lambda;\sigma} \\ &+ \sum_x t_\perp \left(e^{-i2\pi\Phi a_c \tan\theta} c^\dagger_{x,k_y;2;\sigma} c_{x,k_y;1;\sigma} + \text{H.c.} \right)\end{aligned} \tag{5}$$

where a_c is the ratio of inter-bilayer spacing to the in-plane lattice constant. Eq. 5 has three properties that make it particularly amenable to numerical analysis: (i) the two spins $\sigma = \pm 1/2$ are decoupled and can be studied independently; 2) for arbitrary (irrational) values of Φ, the spectrum of H is independent of k_y in the thermodynamic limit[55], allowing us to suppress the k_y summation; 3) the resulting one-dimensional problem concerning $\hat{H}_{k_y,\sigma}$ is a block tri-diagonal matrix, whose inverse (and by extension, the Green's function) can be calculated recursively as described in Appendix C, allowing efficient evaluations of its physical properties on system sizes as large as $L_x \sim 10^7$ sites along the $\hat{x}$ direction. In the remainder of the paper, we will be presenting calculations of QOs in the density of states (DOS) ρ at chemical potential μ, defined as

$$\begin{aligned}\rho(\mu) &= -\frac{1}{\pi L_x} \mathrm{Tr}\left(\mathrm{Im}[\hat{G}] \right) \\ &= -\frac{1}{\pi L_x} \sum_{x,\lambda} \mathrm{Im}[G_{(x,\lambda),(x,\lambda)}(\mu)]\end{aligned} \tag{6}$$

where $G_{(x,\lambda),(x,\lambda)}(\mu)$ represents the diagonal entry of the Green's function

$$\hat{G}(\mu) = \left[(\mu + i\delta)\,\hat{I} - \hat{H}_{k_y,\sigma} \right]^{-1}, \tag{7}$$

The small imaginary term $i\delta$ gives a finite lifetime to the quasiparticles and broadens the Landau levels.

Choice of Parameters

For a range of values, the qualitative aspects of our results do not depend sensitively on the values of most of the parameters that enter the model (with the exception of the pattern of magnetic breakdown, which we shall see is extremely sensitive to the value of $t_\perp$). However, to facilitate comparison with experiment, we chose parameters so that the k-space area enclosed by the elliptical Fermi pockets in the absence of interlayer tunneling is $S_0 \approx 530T = 1.91\%BZ$, the mean cyclotron effective mass $m^* \sim 1.6 m_e$, and the electron's spin g factor is $g = 2$. (See Appendix D for further discussion.) In the absence of any direct experimental information concerning the ellipticity of the Fermi pockets, we have arbitrarily adopted a moderate anisotropy, $\sqrt{3}$ (i.e. the major axis of the ellipse is $\sqrt{3}$ times larger than its minor axis.)

These considerations lead us to take $t_b = t_a/3$, $\tilde{g} = 0.87$ and $\mu = -2.5306 t_a$. Since all our calculations are carried out at $T = 0$, the overall scale of energies is unimportant, but when referring to quantitative features of the electronic structure of YBCO, we will take $t_a = 400$ meV, in which case a characteristic inverse lifetime is $\delta = 0.005 t_a \approx (2\text{ ps})^{-1}$. We convert flux quanta per unit cell, Φ, into units of the actual magnetic field B, by using a unit cell area of YBCO to be $\nu_{\text{unit cell}} = 3.82\text{Å} \times 3.89\text{Å}$. This means that B is related to the flux per unit cell (in units of the flux quantum) by $B = (h/e) \times (\Phi/\nu_{\text{unit cell}}) \approx \Phi \times 27800$. The values of the interlayer tunneling, $t_\perp$, and the inverse lifetime δ are treated as unknowns; exploring the changes in the QO spectrum which occur as they vary is one of the principal purposes of this study.

II. SEMICLASSICAL CONSIDERATIONS

Before undertaking the numerical solution of this model, it is useful to outline the results of a semiclassical analysis to anticipate the basic structure of the QOs

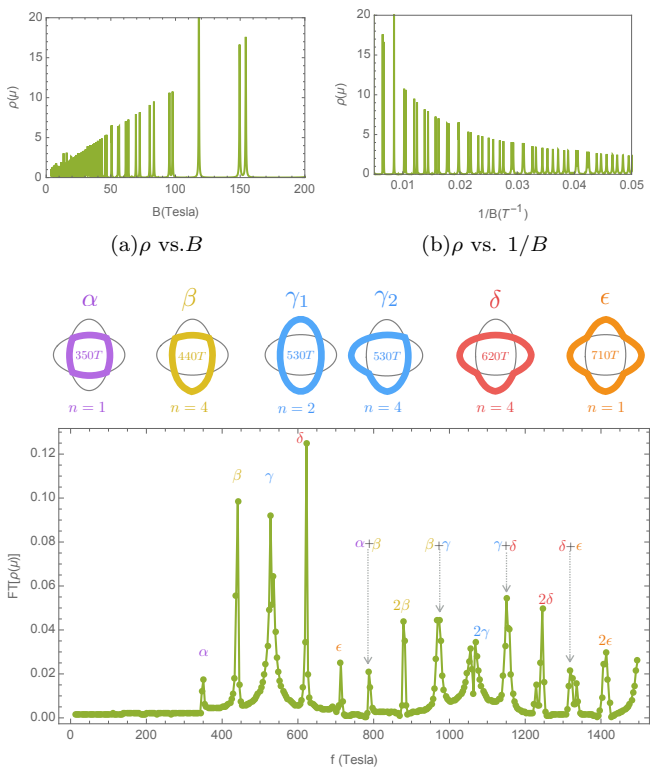

(a)ρ vs.B (b)ρ vs. $1/B$

(c)Fourier transform of (b)

FIG. 3: QOs of the DOS for very small broadening $\delta = 0.0001t_a$ (long lifetimes) and $t_\perp = 0.005t_a$, in the absence of a Zeeman coupling ($\tilde{g} = 0$). Panels (a) and (b) show the calculated DOS ρ vs. B and $1/B$; panel (c) is the Fourier transform of panel (b). Each peak indicates a characteristic frequency of QOs and the corresponding semiclassical orbits are also illustrated above. The number of equivalent semiclassical orbits, n, is indicated below each orbit, and we have explicitly shown the two distinct classes of γ orbits. A relatively large range of magnetic field is used $4T < B < 1000T$ to capture all of the QO frequencies. The system size is $L_x = 2^{23}$.

in the simplest situation in which B is perpendicular to the planes. As we are considering weakly coupled bilayers, we will always assume that $t_\perp \ll t \equiv \sqrt{t_a t_b}$, so the bilayer split Fermi surfaces have narrowly avoided crossings at four symmetry related points, as shown in Fig. 2b. Electrons adhere strictly to semiclassical orbits only so long as $\hbar\omega_c \ll t_\perp^2/t$ since magnetic breakdown at these four points becomes significant otherwise. (Here $\omega_c \sim \phi t$ is the cyclotron frequency.) Taking this magnetic breakdown into account, there are five distinct classes of semiclassical orbits, as shown in the middle panel of Fig. 3, each enclosing a $\boldsymbol{k}$-space area which, when converted into an oscillation frequency, correspond to five oscillation frequencies separated by $\Delta f \approx 90T$ for the model parameters we have defined. (These correspond to the frequencies labeled α, β,γ, δ, and ϵ in the spectrum in the lower panel of the figure, whose calculation is discussed in the next section).

The largest and smallest orbits represent the true

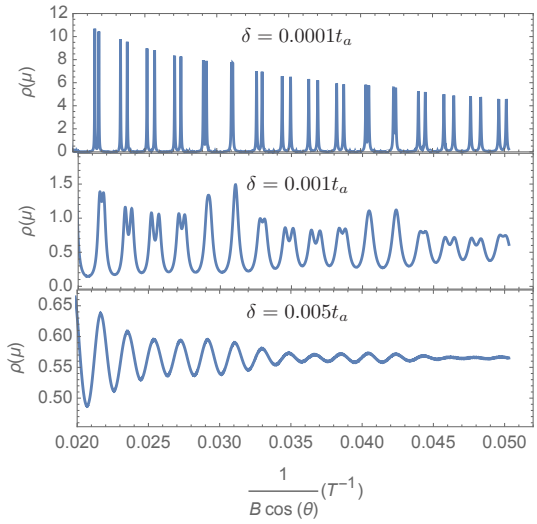

FIG. 4: The evolution of QOs in the DOS $\rho(\mu)$ for various values of the inverse quasiparticle lifetime, δ. The interlayer tunneling $t_\perp = 0.005t_a$ and the rest of the parameters are detailed at the end of Sec. I.

structure of the Fermi surface, so these two frequencies (α and ϵ) must dominate the QO spectrum when $\hbar\omega_c \ll t_\perp^2/t$. Conversely, in the limit $\hbar\omega_c \gg t_\perp^2/t$, where to good approximation we can set $t_\perp = 0$, the spectrum is dominated by the central frequency (γ_1), in which the electron orbits are confined to a single plane of the bilayer, and hence correspond to the ellipses in Fig. 2a.[69] More complex spectra, including those with the three peak structure seen in experiment, occur only when $\hbar\omega \sim t_\perp^2/t$. This, we shall see, allows us to estimate the magnitude of $t_\perp$ directly from experiment.

We will return again to a semiclassical analysis, below, in order to understand still more subtle features of the QO spectrum which appear when the magnetic field is tilted relative to the Cu-O plane.

III. NUMERICAL RESULTS

In presenting our results, we will adopt two complementary approaches. We first study an idealized theoretical limit of infinitesimally small broadening ($\delta \to 0$, i.e. infinite quasiparticle lifetime) and without Zeeman splitting, where a sharp Landau level structure of the density of states is present and easy to interpret. These numerical 'experiments' are done for a very large range of field strengths. We subsequently study the model over an experimentally realistic range of magnetic fields with the inclusion of Zeeman splitting, while tuning the broadening and interlayer tunneling $t_\perp$, and subsequently examining the angular dependences. While we predominantly highlight the robust qualitative features of this model, we also focus on the quantitative aspects of magnetic breakdown, which are treated exactly in our numerical studies.

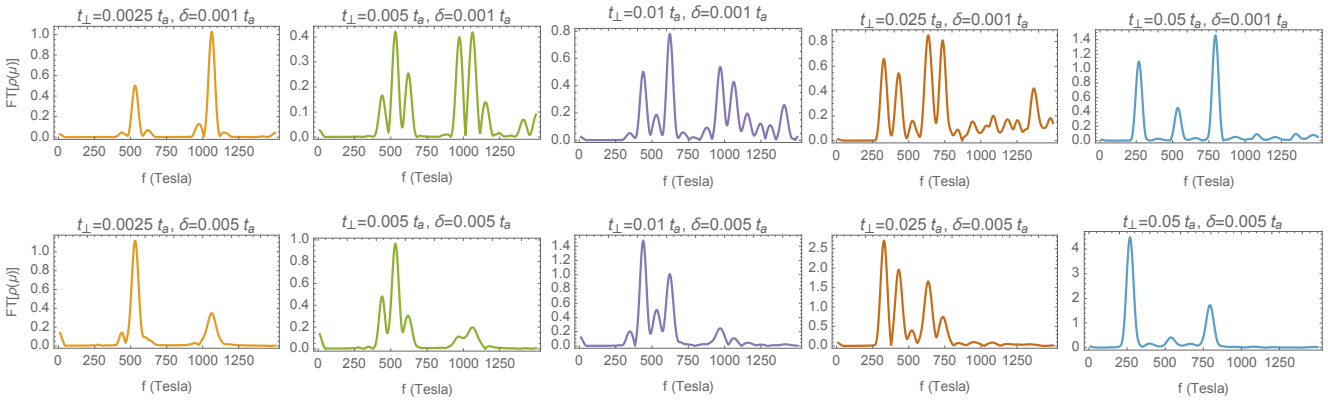

FIG. 5: The raw Fourier transform of the density of states oscillations as the interlayer tunneling $t_\perp$ is increased (left to right), and the inverse lifetime δ is increased (top to bottom). Larger values of $t_\perp$ suppress the central frequencies and enhance the satellite frequencies which correspond to orbits of the true bilayer split Fermi surface. Shorter quasiparticle lifetimes (larger δ) lead to decreased harmonic content. The field range used here is $20T < B < 100T$, with 2^{10} data points.

In Fig. 3 we show the density of states as a function of magnetic field strengths for a c-directed field. The top panels show data where the broadening is infinitesimal at $\delta = 0.0001t_a$ and there is no Zeeman splitting. Each Landau level is split due to the presence of two coupled layers, while the peaks in the density of states rise linearly with B as expected for free fermions. The lower panel of Fig. 3 shows the Fourier transform of this data over a large range of magnetic fields ($4T < B < 1000T$). Here the high harmonic content of the oscillations is clearly seen, with comparable-in-magnitude first and second harmonics. For the first harmonics, there are five peaks clustered around a central frequency of $f = 530T$, as expected from semiclassical considerations, while at higher frequencies there are all the expected harmonic combinations giving rise to a complicated spectrum.

A. Dependence on interlayer tunneling and lifetime

We now study the model over an experimentally realistic range of magnetic fields with a finite Zeeman coupling, $\tilde{g} = 0.87$. Fig. 4 and 5 show the evolution of the QOs as the interlayer tunneling $t_\perp$ and Landau level broadening δ are varied, where we have reduced the range of magnetic field to $20T < B < 100T$ to conform roughly with the range explored by current experiments in YBCO. The figures are constructed from 2^{10} data points. As is clear from Fig. 4 the form of the oscillations is radically altered as the lifetime is decreased (δ in Eq. 7 is increased), with the sharp Landau level structure of the spectrum becoming broadened. This leads to oscillations with little harmonic content, while the amplitude of the oscillatory signal is also sharply suppressed.

Fig. 5 shows the Fourier transform[70] of ρ as both the interlayer tunneling $t_\perp$ is increased (from left to right) and the inverse lifetime δ is increased (from top to bottom). Several qualitative features of the results are immediately apparent. (1) As the inverse lifetime δ is increased (and the oscillations of ρ become less singular), the peaks in the Fourier transform are also broadened while the higher frequency peaks are preferentially suppressed in amplitude, leading to oscillations with little harmonic content. This has a simple semiclassical interpretation: higher frequency peaks correspond to longer semiclassical orbits and so are suppressed in amplitude by the decreasing quasiparticle lifetime.[56] (2) The competition between different semiclassical orbits is sensitively controlled by the interlayer tunneling $t_\perp$: as $t_\perp$ is increased, the gaps between bonding and anti-bonding Fermi surfaces increase, and the weight of QOs rapidly shifts from the central frequency at $530T$ (corresponding to the 3rd orbit in Fig. 3 which involves two magnetic breakdowns across the true Fermi surface of the bilayer) to the side frequencies at $(530 \pm 90)T$ (corresponding to the second and fourth semiclassical orbits in Fig. 3), and is eventually dominated by the outermost frequencies at $(530 \pm 180)T$ (reflecting the 'true' bonding and anti-bonding Fermi surfaces of the bilayer).

Indeed, a particularly appealing feature of our approach is its exact treatment of magnetic breakdown. The immediate quantitative observation from Fig. 5 is that maintaining the large (experimentally observed) ratio of the amplitude of the central $530T$ frequency to that of the satellite frequencies at $530 \pm 90T$ requires very small values of the interlayer tunneling $t_\perp < 0.01t_a$. This is at least an order of magnitude below the typical values of $t_\perp \sim 0.1t_a$ assigned by band structure studies[48,49] and ARPES studies[51] on overdoped YBCO, but agrees remarkably with ARPES measurements of the underdoped regime. We discuss the consequences of this observation in Sec. IV.

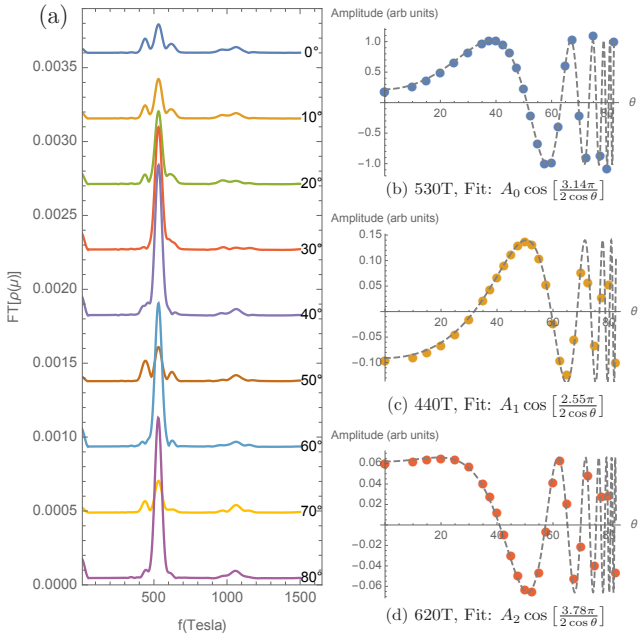

FIG. 6: (a) The Fourier transform of the DOS QOs for various polar angles θ of the magnetic field $\vec{B}$ (different angles have been arbitrarily offset). (b)-(d) Extracted peak heights in the Fourier transform (we have used both amplitude and phase information) versus the polar angle θ. The parameters are $\delta = 0.005t_a$, $t_\perp = 0.005t_a$. The dashed lines are the theoretical fits of the angular dependence due to spin splitting (Eq. 8) which is caused by Zeeman effect.

B. Polar angle (θ) dependence of the QOs

We now move on to cases where the magnetic field is tilted away from the principal c-axis of this model and study the dependence of the QOs on the polar and azimuthal angles, θ and ϕ; we also comment briefly on the corresponding dependence seen in YBCO. Key experimental features include the presence of spin zeros near $\theta \approx 51.5°$ and $\theta \approx 63.5°$, with the notable absence of a Yamaji angle that is typical of simple s-wave warping of a three dimensional Fermi surface. Spin zeros (as well as the general θ dependence) arise due to Zeeman splitting of spinful electrons. This coupling effectively shifts the chemical potential (and hence the area of each orbit) oppositely for each species σ, by an amount that is proportional to the applied field $\delta f = \sigma\gamma B$. Such a B dependent shift of the Fermi surface area for each spin species becomes a shift of the bare (spinless) frequency f_0 of oscillations, so that the amplitude of oscillations for the p'th harmonic acquires a field independent (but θ dependent) factor:

$$\rho\left(\frac{1}{B},\theta\right) \propto \sum_{\sigma=\pm 1/2} \cos\left(2\pi p \frac{(f_0+\sigma\gamma B)}{B\cos\theta}\right) = 2\cos\left(\frac{\pi p\gamma}{\cos\theta}\right)\cos\left(2\pi p\frac{f_0}{B}\right). \quad (8)$$

A more careful analysis shows that this field independent amplitude takes the form $A(\theta) = \cos\left(\pi p g \frac{m^*}{2m_e\cos\theta}\right)$ where in practice the factor $\pi p g m^*/2m_e$ is related to our definition of $\tilde{g}$ as discussed in Appendix D.

Fig. 6(a) shows the polar angle θ dependence of the Fourier transform of QOs for the model system in Eq. 1. The azimuthal angle is fixed at $\phi = 45°$ throughout the calculation. As expected, no Yamaji-like resonance is seen because of the absence of a truly three-dimensional dispersion. Fig. 6(b)-(d) shows the θ dependence of the QO amplitude $A(\theta)$ at the three main frequencies. We see characteristic spin-zeros in the primary frequency $f = 530T$ near $\theta_0 = 51.5°$ and $\theta_1 = 63.5°$. The dashed lines show fits of the amplitude to the form given in Eq. 8 - remarkable agreement is found. We note that the positions of the spin zeros are different for the QOs at frequencies $440T$, $530T$ and $620T$, despite the fact that the g-factor (our parameter $\tilde{g}$) has been defined to be the same for all orbits. This robust feature of our model can be attributed to the different effective mass of these three orbits which enters the formula $\cos(\pi p g m^*/2m_e\cos\theta)$, and is explored further in Appendix D.

C. Azimuthal angle (ϕ) dependence of the QOs

Another notable feature of QO experiments in YBCO is the dependence of the amplitude of the oscillations on the azimuthal angle ϕ. The oscillation amplitudes exhibit a four-fold anisotropy, which increases with increasing polar angle θ. Here, we show that these features can be reproduced in our model of a single bilayer, with the caveat that strong anisotropy is only natural for selected orbits that involve both layers of the bilayer (β orbit at $440T$, δ orbit at $620T$ and γ_2 orbit at $530T$).

In analyzing the behavior of QOs for different azimuthal angles, much information can be gleaned from semiclassical intuitions. First, note that the semiclassical orbits γ_1 at the central $530T$ frequency in Fig. 3 are predominantly confined to a single layer of the bilayer. Such 2d orbits are only affected by the field perpendicular to the layer, therefore no observable azimuthal dependence is expected. On the other hand, all other semiclassical orbits shown in Fig. 3 involve tunneling events from one layer to the next, upon which electrons may obtain a phase proportional to the horizontal magnetic field $B\sin\theta$. This means that there is weak four-fold dependence arising from γ_2 orbits, wherever the signal is dominated by the $530T$ frequency; conversely, a large four-fold modulation arises from the $530 \pm 90T$ frequencies, and so

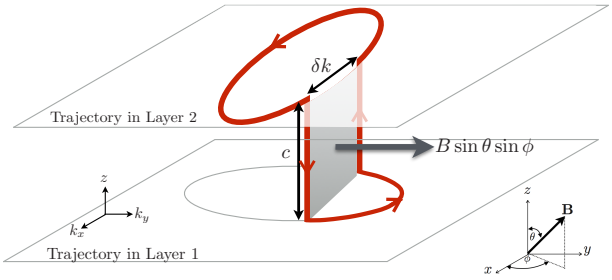

(a)3D Cartoon plot of semiclassical orbit in the bilayer

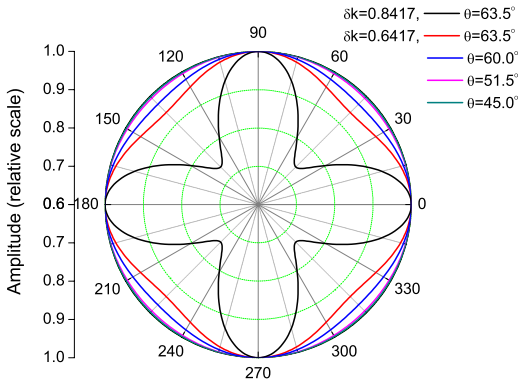

(b)Corresponding ϕ dependence of the QOs at $620T$ and $440T$ given in Eq. 9

FIG. 7: (a) A schematic diagram showing how the in-plane component of the flux enclosed by a given semiclassical orbit (δ orbit in Fig. 3) is determined. The red curve is the semiclassical orbit, while grey ellipses are the Fermi surfaces. Note that the in-plane directions are in momentum space, while the vertical separation is in real space. The vertical region enclosed (shaded gray) has a (real space) area of $\delta k \ell_B^2 c$. (b) The ϕ dependence of QO amplitude $A_1(\phi)$ as in Eq. 9 for various values of the polar angle θ for $\delta k = 0.6417$ defined in our model as well as the case of a larger $\delta k = 0.8417$. The anisotropy is clearly more apparent for larger θ and/or δk.

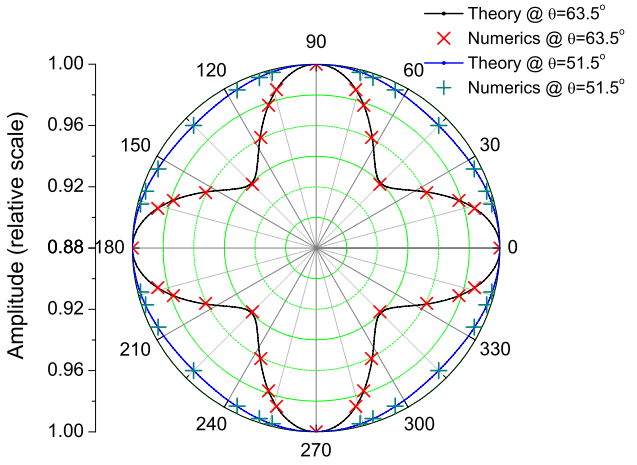

FIG. 8: The relative amplitude of the QOs at frequency $620T$ for polar angles $\theta = 63.5°$ and $\theta = 51.5°$, respectively. The QO amplitude at $\phi = 0$ is maximal and set as the unit 1 for each of the data sets. The solid curve is the theoretical expectation value according to Eq. 9 and the expected C_4 rotation symmetry is clearly present. The parameters used in our numerical calculations of the DOS QOs are $t_\perp = 0.005$, $\delta = 0.001$ and $11T < B < 100T$.

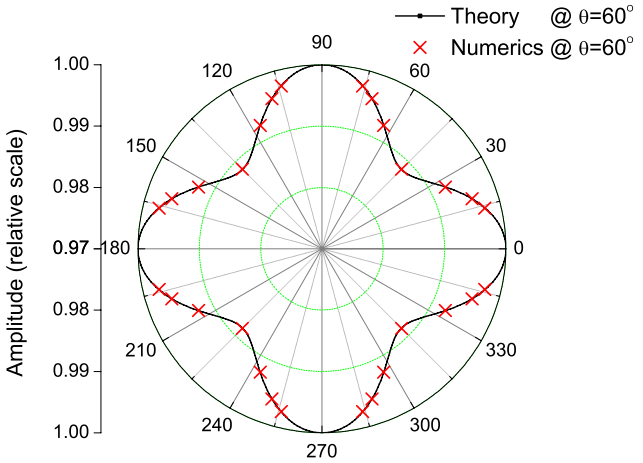

FIG. 9: The relative amplitude of the QOs at frequency $530T$ for polar angles $\theta = 60°$. The solid curve is the fit to theoretical form given by Eq. 10 with $M = -13.5$. The parameters used in our numerical calculations of the DOS QOs are $t_\perp = 0.005$, $\delta = 0.001$ and $11T < B < 100T$.

is pronounced near to spin zero angles $\{\theta_0, \theta_1\}$ of the main $530T$ frequency.

Within the semiclassical framework, we can obtain an analytic expression for the amplitude as a function of azimuthal angle ϕ by determining the amount of in-plane directed magnetic flux enclosed by a given breakdown orbit. Fig 7(a) shows the geometry of a particular breakdown orbit for QOs at $620T$, where the total horizontal flux is the real space area corresponding to the shaded region, multiplied by the field component $B\sin\theta\sin\phi$. Semiclassically, we find the real space area enclosed by the orbit to be $\delta k \ell_B^2 c$, where $\ell_B^2 = h/eB\cos\theta$ is the square of the magnetic length, and δk is the distance between the (avoided) crossings of the Fermi surfaces (see Fig. 7(a)). Thus, the in-plane flux enclosed by this orbit is $\Phi_{yz} = \delta k \frac{\hbar}{eB} c \times B\tan\theta\cos\phi = c\delta k \tan\theta \sin\phi$ with our choices of units. Similarly, there are three other possible enclosed fluxes related by C_4 rotations and given by $\Phi_{-yz} = -\Phi_{yz}$, and $\Phi_{\pm xz} = \pm c\delta k \tan\theta\cos\phi$. The resulting Φ_j, $j = \pm xz, \pm yz$ each give an additional constant initial phase to the in-plane fluxes that determine the QOs of the corresponding reconstruction, which add up

to give the overall amplitude:

$$A_1(\phi) \propto \sum_j \exp\left(i\Phi_j\right) \propto 2\cos\Phi_{xz} + 2\cos\Phi_{yz} \quad (9)$$
$$\propto 2\cos\left(c\delta k \tan\theta\cos\phi\right) + 2\cos\left(c\delta k\tan\theta\sin\phi\right)$$

Examples of the azimuthal angular dependence given by Eq. 9 are shown in Fig. 7(b), whose form confirms C_4 rotation symmetry. For smaller values of the polar angle θ (and thus a smaller overall factor $c\delta k\tan\theta$), the ϕ angular dependence is suppressed. We note that the magnitude of the anisotropy depends sensitively on δk. An example of the QO amplitude variation for a larger $\delta k = 0.8417$ as compared to the original $\delta k = 0.6417$ is also included in Fig. 7(b).

It is straightforward to verify that the angular dependence of the QOs at $440T$ has the same result as Eq. 9, while at $530T$ we need to consider both the γ_1 and γ_2 orbits:

$$A_1'(\phi) \propto M + 2\cos\left(c\delta k\tan\theta(\cos\phi+\sin\phi)\right)$$
$$+ 2\cos\left(c\delta k\tan\theta(\cos\phi-\sin\phi)\right) \quad (10)$$

where M is a complex constant for the contribution from γ_1 orbits which sensitively depends on the parameters including $t_\perp$ and B.

Another immediate consequence of this expression is that the maximum in QO amplitudes at the side frequencies at $(530 \pm 90)T$ occurs when the field is aligned with the principal axes of the ellipses. Given that experimentally, the maximum of the oscillation amplitudes is seen to occur for fields along the a and b crystallographic directions, it is natural that the principal axes of such elliptical pockets must lie along the a and b directions, i.e. such azimuthal dependence seemingly rules out proposals where the principal axes of the Fermi pockets are oriented at 45° to the a and b crystallographic directions.

Returning to the model at hand, we calculated numerically the density of states QOs with selected values of the azimuthal angle $\tan\phi = 0, 1, 2, 3, 4$ (plus symmetry related values) and various polar angles. The resulting QO amplitudes at frequency $620T$ and polar angles $\theta = 63.5°$ and $\theta = 51.5°$ are shown in Fig. 8 and are fully consistent with the semiclassical expression derived in Eq. 9. In particular, the selected θ values are the spin zeros of the central frequency at $f = 530T$ of the QOs, where the effect of the side frequencies at $(530\pm90)T$ are enhanced. In addition, four-fold anisotropy is also seen for the QO amplitudes at frequency $530T$ and polar angle $\theta = 60°$ as shown in Fig. 9. It fits well to Eq. 10 with parameter $M = -13.5$.

IV. IMPLICATIONS FOR THE CUPRATES

We have shown that a simple model of criss-crossed elliptical electron pockets can reasonably account for the most striking experimental observations of QOs in the bilayer cuprate YBCO. In particular, we have shown that a three peak structure in the Fourier transform of QOs follows naturally from the ansatz of broken mirror symmetry[71] and weak bilayer splitting. The choices of tight-binding and Zeeman-splitting parameters that best capture this physics have been analyzed semi-quantitatively. We have also demonstrated that major features of both the azimuthal and polar angular dependence of the QOs can be qualitatively reproduced by this simplified model of a single bilayer.

A central feature of our analysis involves the small effective interlayer tunneling $t_\perp$ required to account for the prominence of the central $530T$ frequency relative to those at $530 \pm 90T$. In certain situations, a singular k dependence[48,49,57] of the bare interlayer tunneling, $t_\perp^{(0)}(k) \approx t_\perp^{(0)}(\cos k_x - \cos k_y)^2$, arises due to the local quantum chemistry. In this case the small value of the effective $t_\perp$ could reflect the location of the electron pockets along the "nodal" direction in the Brillouin zone where $|k_x| = |k_y|$, rather than any non-trivial many-body effect. However, there are strong reasons to doubt that the bilayer tunneling in YBCO has such strong k dependence. On theoretical grounds, LDA studies[48,49] have found that the tunneling between the 'dimpled' planes of a YBCO bilayer remains substantial even along the nodal direction with $t_\perp^{(0)}(\boldsymbol{k}_n) \approx 120$meV, compared to an antinodal value of $t_\perp^{(0)}(\boldsymbol{k}_{an}) \approx 150$meV.

This LDA prediction is supported by ARPES measurements on YBCO in the overdoped regime[51] where an almost isotropic bilayer splitting of $\Delta\varepsilon_{\boldsymbol{k}_n} = 2t_\perp(\boldsymbol{k}_n) = 2Zt_\perp^{(0)}(\boldsymbol{k}_n) \approx 130$meV in the nodal direction, compared to an antinodal splitting $\Delta\varepsilon_{\boldsymbol{k}_{an}} \approx 150$meV leads to a near isotropic quasiparticle weight of $Z \approx 0.5$. This is in sharp contrast to underdoped samples, where despite the theoretical (LDA) prediction of a doping independent $t_\perp^{(0)}$, the nodal bilayer splitting is difficult to resolve. These experiments give an upper bound of the nodal quasiparticle weight in the underdoped regime of $Z_n < 0.065$, while an estimate based on the rescaled values of the spectral weight yields $Z_n \approx 0.03$. Such estimates agree remarkably well with our estimate of the effective value of $t_\perp$ necessary to account for the QO's in underdoped YBCO. The constraint of the quasiparticle weight $\tilde{Z} \lesssim 0.05$, strongly suggests that the effective Fermi liquid parameter $t_\perp = \tilde{Z}t_\perp^{(0)}$ is renormalized significantly downwards.

A. Comparison with previous proposals

There have been many proposals[32–43] for the origin of the Fermi surface reconstruction in the cuprates. Given recent observations of (seemingly ubiquitous[16–31]) incommensurate CDW order, a prime candidate for the Fermi surface is one where nodally located electron pockets are produced by incommensurate CDWs which are at least bi-axial, involving ordering at $\vec{Q}_x = (Q, 0, 1/2)$

and $\vec{Q}_y = (0, Q, 1/2)$. This idea, along with the invocation of breakdown orbits due to bilayer splitting to account for the three peak structure of the Fourier transform, was first advanced by Harrison, Sebastian and coworkers[10,34]. In this scenario, a diamond shaped, nodally located electron pocket is split by bilayer tunneling (with the above mentioned $(\cos k_x - \cos k_y)^2$ form factor), with all three observed frequencies involving orbits where the electron tunnels from one layer to the next. The nodal location also serves to suppress simple isotropic (s-wave) hopping in the c axis direction, leading to an absence of a Yamaji resonance.

The model discussed in the present paper, while similar in spirit to that of Harrison and Sebastian, possesses crucial differences of symmetry and effective dimensionality. Under the assumption that QO experiments probe the physics of a single bilayer, mirror symmetry between the two layers of this bilayer must be broken in order for breakdown orbits to be present in a purely c-axis directed magnetic field – otherwise a conserved bilayer parity associated with the split Fermi surfaces would prevent all magnetic breakdown (see Appendix B). Indeed, there is evidence for such broken symmetry in the low field charge order.[31,42] Once mirror symmetry is broken, a natural consequence is that the central $530T$ frequency reflects a semiclassical orbit where electrons are confined to a single layer of the bilayer, and if so, is naturally the most prominent in the regime of small interlayer tunneling.[72] We have demonstrated that the experimental observations can be generally accounted for in the context of a minimal model of a single bilayer. In contrast to previous proposals, this model requires no specific $3d$-structure of the Fermi surface, and makes no specific assumptions about the nature of the order that reconstructs the Fermi surface. With the recent high field X-ray scattering experiments[58] giving evidence of an unexpected, distinct high-field character of the CDW order, we view this lack of specificity as a virtue.

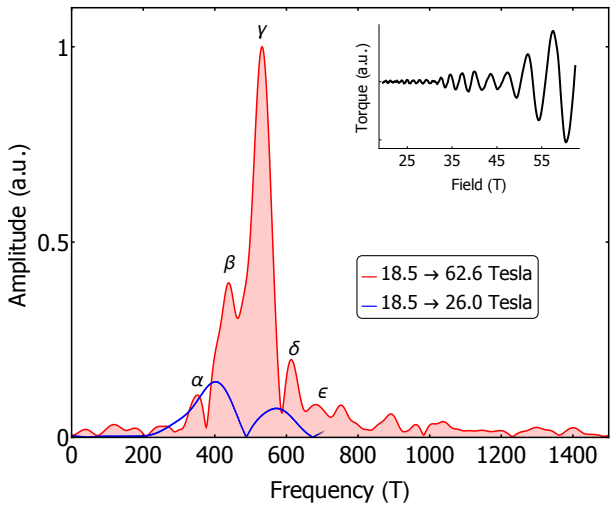

FIG. 10: Fourier transform of torque quantum oscillation in $YBa_2Cu_3O_{6.58}$. Analysis of the full field range, from 18.5 to $62.6T$ (red curve), reveals spectral features not present in Fig. 1, but that correspond well with the frequencies shown in Fig. 3. Analysis of the oscillations between 18.5 and $26T$ only (blue curve) shows that spectral weight is shifted away from the main γ peak, and toward the side lobes. The blue curve has been multiplied by a factor of 10 and truncated at $700T$ for clarity. Note that spectral features below $\approx 150T$ are removed as part of the background-subtraction procedure, and thus this data does not address the possibility of a $90T$ frequency that has been reported in transport measurements[46].

B. Further tests from experiments in $YBa_2Cu_3O_{6.58}$

The magnetic breakdown scenario makes two specific predictions for QO experiments in bilayer cuprates:

1. Oscillations taken over a sufficiently large field range should show five spectral features distributed symmetrically about the main frequency, plus multiple higher harmonics from combination orbits.

2. The weight of the various frequency components of the quantum oscillations should be field-dependent, with orbits that require fewer breakdown events dominating at low fields.

Fig. 10 shows torque magnetometry data taken on $YBa_2Cu_3O_{6.58}$ at $1.5K$. Multiple spectral components, beyond the three main peaks identified in previous studies but consistent with those presented in section III, are clearly visible with this extended field range (18.5 to $62.6T$). Appendix E demonstrates that these peaks (particularly α and ϵ) are not artifacts of the Fourier transform, but are instead physical components of the oscillatory signal.

Transforming the data over a limited low-field range, from 18.5 to $26T$ (blue curve in Fig. 10), shows that the main $530T$ peak is indeed no longer dominant. Semiclassically[59], the probability of tunneling through any one of the four junctions between the bilayer split Fermi surfaces (Fig. 2) is $P = e^{-B_0/B}$, where B_0 is the characteristic breakdown field. The probability of avoiding breakdown (Bragg reflection) at a junction is $(1-P)$. While this expression is not exact (unlike the breakdown treatment in Section III), particularly at fields large compared to B_0, it gives intuition as to why the spectral weight shifts at lower fields: the γ orbit shown in Fig. 3 requires four breakdown events, while the α (ϵ) orbit requires none and the β (δ) orbit requires two. Note that the field range used to obtain the blue curve in Fig. 10 is insufficient to resolve the splitting of these peaks. Finally, the dominance in amplitude of lower frequencies over higher frequencies originates[56] in the suppression of larger orbits due to quasiparticle scattering[73].

V. ACKNOWLEDGEMENTS

We acknowledge extremely useful discussions with A. Damascelli, N. Harrison, G. Lonzarich, A. P. Mackenzie, C. Proust, S. Sebastian, L. Taillefer and J. Tranquada. This work was supported in part by the US Department of Energy, Office of Basic Energy Sciences under contract DE-AC02-76SF00515 (A.V.M.), Stanford Institute for Theoretical Physics (Y.Z.), the US Department of Energy Office of Basic Energy Sciences "Science at 100 T," (B.J.R.) and the National Science Foundation through Grant No. DMR 1265593 (S.A.K.). The National High Magnetic Field Laboratory facility is funded by the Department of Energy, the State of Florida, and the NSF under cooperative agreement DMR-1157490 (B.J.R).

[1] N. Doiron-Leyraud, C. Proust, D. LeBoeuf, J. Levallois, J. Bonnemaison, R. Liang, D. Bonn, W. Hardy, and L. Taillefer, Nature **447**, 565 (2007).
[2] D. LeBoeuf, N. Doiron-Leyraud, J. Levallois, R. Daou, J.-B. Bonnemaison, N. Hussey, L. Balicas, B. Ramshaw, R. Liang, D. Bonn, et al., Nature **450**, 533 (2007).
[3] A. Bangura, J. Fletcher, A. Carrington, J. Levallois, M. Nardone, B. Vignolle, P. Heard, N. Doiron-Leyraud, D. LeBoeuf, L. Taillefer, et al., Physical Review Letters **100**, 047004 (2008).
[4] E. Yelland, J. Singleton, C. Mielke, N. Harrison, F. Balakirev, B. Dabrowski, and J. Cooper, Physical Review Letters **100**, 047003 (2008).
[5] B. Vignolle, A. Carrington, R. Cooper, M. French, A. Mackenzie, C. Jaudet, D. Vignolles, C. Proust, and N. Hussey, Nature **455**, 952 (2008).
[6] A. Audouard, C. Jaudet, D. Vignolles, R. Liang, D. Bonn, W. Hardy, L. Taillefer, and C. Proust, Physical Review Letters **103**, 157003 (2009).
[7] S. E. Sebastian, N. Harrison, P. Goddard, M. Altarawneh, C. Mielke, R. Liang, D. Bonn, W. Hardy, O. Andersen, and G. Lonzarich, Physical Review B **81**, 214524 (2010).
[8] J. Singleton, C. de La Cruz, R. McDonald, S. Li, M. Altarawneh, P. Goddard, I. Franke, D. Rickel, C. Mielke, X. Yao, et al., Physical Review Letters **104**, 086403 (2010).
[9] B. Ramshaw, B. Vignolle, J. Day, R. Liang, W. Hardy, C. Proust, and D. Bonn, Nature Physics **7**, 234 (2011).
[10] S. E. Sebastian, N. Harrison, R. Liang, D. Bonn, W. Hardy, C. Mielke, and G. Lonzarich, Physical Review Letters **108**, 196403 (2012).
[11] S. E. Sebastian, N. Harrison, and G. G. Lonzarich, Reports on Progress in Physics **75**, 102501 (2012).
[12] N. Barišić, S. Badoux, M. K. Chan, C. Dorow, W. Tabis, B. Vignolle, G. Yu, J. Béard, X. Zhao, C. Proust, et al., Nature Physics **9**, 761 (2013).
[13] S. E. Sebastian, N. Harrison, F. Balakirev, M. Altarawneh, P. Goddard, R. Liang, D. Bonn, W. Hardy, and G. Lonzarich, Nature **511**, 61 (2014).
[14] S. E. Sebastian and C. Proust, Annu. Rev. Condens. Matter Phys. **6**, 411 (2015).
[15] B. Ramshaw, S. Sebastian, R. McDonald, J. Day, B. Tan, Z. Zhu, J. Betts, R. Liang, D. Bonn, W. Hardy, et al., Science **348**, 317 (2015).
[16] J. Tranquada, D. Buttrey, V. Sachan, and J. Lorenzo, Physical Review Letters **73**, 1003 (1994).
[17] J. Tranquada, B. Sternlieb, J. Axe, Y. Nakamura, and S. Uchida (1995).
[18] M. Fujita, H. Goka, K. Yamada, J. Tranquada, and L. Regnault, Physical Review B **70**, 104517 (2004).
[19] C. Howald, H. Eisaki, N. Kaneko, M. Greven, and A. Kapitulnik, Physical Review B **67**, 014533 (2003).
[20] J. Hoffman, E. Hudson, K. Lang, V. Madhavan, H. Eisaki, S. Uchida, and J. Davis, Science **295**, 466 (2002).
[21] T. Hanaguri, C. Lupien, Y. Kohsaka, D.-H. Lee, M. Azuma, M. Takano, H. Takagi, and J. Davis, Nature **430**, 1001 (2004).
[22] J. Fink, E. Schierle, E. Weschke, J. Geck, D. Hawthorn, V. Soltwisch, H. Wadati, H.-H. Wu, H. A. Dürr, N. Wizent, et al., Physical Review B **79**, 100502 (2009).
[23] F. Laliberté, J. Chang, N. Doiron-Leyraud, E. Hassinger, R. Daou, M. Rondeau, B. Ramshaw, R. Liang, D. Bonn, W. Hardy, et al., Nature Communications **2**, 432 (2011).
[24] J. Chang, E. Blackburn, A. Holmes, N. Christensen, J. Larsen, J. Mesot, R. Liang, D. Bonn, W. Hardy, A. Watenphul, et al., Nature Physics **8**, 871 (2012).
[25] G. Ghiringhelli, M. Le Tacon, M. Minola, S. Blanco-Canosa, C. Mazzoli, N. Brookes, G. De Luca, A. Frano, D. Hawthorn, F. He, et al., Science **337**, 821 (2012).
[26] A. J. Achkar, R. Sutarto, X. Mao, F. He, A. Frano, S. Blanco-Canosa, M. Le Tacon, G. Ghiringhelli, L. Braicovich, M. Minola, et al., Phys. Rev. Lett. **109**, 167001 (2012).
[27] N. Doiron-Leyraud, S. Lepault, O. Cyr-Choiniere, B. Vignolle, G. Grissonnanche, F. Laliberté, J. Chang, N. Barišić, M. Chan, L. Ji, et al., Physical Review X **3**, 021019 (2013).
[28] D. LeBoeuf, S. Krämer, W. Hardy, R. Liang, D. Bonn, and C. Proust, Nature Physics **9**, 79 (2013).
[29] Y. He, Y. Yin, M. Zech, A. Soumyanarayanan, M. M. Yee, T. Williams, M. Boyer, K. Chatterjee, W. Wise, I. Zeljkovic, et al., Science **344**, 608 (2014).
[30] W. Tabis, Y. Li, M. Le Tacon, L. Braicovich, A. Kreyssig, M. Minola, G. Dellea, E. Weschke, M. Veit, M. Ramazanoglu, et al., Nature Communications **5** (2014).
[31] E. Forgan, E. Blackburn, A. Holmes, A. Briffa, J. Chang, L. Bouchenoire, S. Brown, R. Liang, D. Bonn, W. Hardy, et al., Nature communications **6** (2015).
[32] S. Chakravarty, R. B. Laughlin, D. K. Morr, and C. Nayak, Phys. Rev. B **63**, 094503 (2001).
[33] A. J. Millis and M. Norman, Physical Review B **76**, 220503 (2007).
[34] N. Harrison and S. Sebastian, Physical Review Letters **106**, 226402 (2011).
[35] J. Eun, Z. Wang, and S. Chakravarty, Proceedings of the National Academy of Sciences **109**, 13198 (2012).
[36] N. Harrison and S. Sebastian, New Journal of Physics **14**, 095023 (2012).
[37] P. A. Lee, Physical Review X **4**, 031017 (2014).
[38] A. Allais, D. Chowdhury, and S. Sachdev, Nature Communications **5** (2014).
[39] Y. Wang and A. Chubukov, Physical Review B **90**, 035149 (2014).
[40] A. V. Maharaj, P. Hosur, and S. Raghu, Phys. Rev. B **90**,

125108 (2014), URL http://link.aps.org/doi/10.1103/PhysRevB.90.125108.
[41] A. Russo and S. Chakravarty, arXiv preprint arXiv:1504.03378 (2015).
[42] A. Briffa, E. Blackburn, S. Hayden, E. Yelland, L. M.W., and E. Forgan, arXiv:1510.02603 (2015).
[43] N. Harrison, B. Ramshaw, and A. Shekhter, Scientific Reports **5** (2015).
[44] H. Yao, D.-H. Lee, and S. Kivelson, Physical Review B **84**, 012507 (2011).
[45] S. C. Riggs, O. Vafek, J. Kemper, J. Betts, A. Migliori, F. Balakirev, W. Hardy, R. Liang, D. Bonn, and G. Boebinger, Nature Physics **7**, 332 (2011).
[46] N. Doiron-Leyraud, S. Badoux, S. R. de Cotret, S. Lepault, D. LeBoeuf, F. Laliberté, E. Hassinger, B. Ramshaw, D. Bonn, W. Hardy, et al., Nature Communications **6** (2015).
[47] Z. Wang and S. Chakravarty, arXiv preprint arXiv:1509.00494 (2015).
[48] O. Andersen, A. Liechtenstein, O. Jepsen, and F. Paulsen, Journal of Physics and Chemistry of Solids **56**, 1573 (1995).
[49] I. Elfimov, G. Sawatzky, and A. Damascelli, Physical Review B **77**, 060504 (2008).
[50] D. Garcia-Aldea and S. Chakravarty, New Journal of Physics **12**, 105005 (2010).
[51] D. Fournier, G. Levy, Y. Pennec, J. McChesney, A. Bostwick, E. Rotenberg, R. Liang, W. Hardy, D. Bonn, I. Elfimov, et al., Nature Physics **6**, 905 (2010).
[52] S. Chakravarty, H.-Y. Kee, and E. Abrahams, Physical Review Letters **82**, 2366 (1999).
[53] L. Ioffe and A. Millis, Science **285**, 1241 (1999).
[54] E. Carlson, D. Orgad, S. Kivelson, and V. Emery, Physical Review B **62**, 3422 (2000).
[55] Y. Zhang, A. V. Maharaj, and S. Kivelson, Physical Review B **91**, 085105 (2015).
[56] C. Bergemann, A. Mackenzie, S. Julian, D. Forsythe, and E. Ohmichi, Advances in Physics **52**, 639 (2003), ISSN 0001-8732.
[57] S. Chakravarty, A. Sudbø, P. W. Anderson, and S. Strong, Science **261**, 337 (1993).
[58] S. Gerber, H. Jang, H. Nojiri, S. Matsuzawa, H. Yasumura, D. A. Bonn, R. Liang, W. N. Hardy, Z. Islam, A. Mehta, et al., Science (2015).
[59] D. Shoenberg, *Magnetic oscillations in metals*, Cambridge monographs on physics (Cambridge University Press, 1984), ISBN 9780521224802.
[60] R. Comin, R. Sutarto, F. He, E. da Silva Neto, L. Chauviere, A. Frano, R. Liang, W. Hardy, D. Bonn, Y. Yoshida, et al., Nature Materials (2015).
[61] D. Chowdhury and S. Sachdev, Physical Review B **91**, 115123 (2015).
[62] D. Chowdhury and S. Sachdev, Phys. Rev. B **90**, 245136 (2014).
[63] P. Hlobil, A. V. Maharaj, P. Hosur, M. Shapiro, I. Fisher, and S. Raghu, Physical Review B **92**, 035148 (2015).
[64] "Bidirectional" here refers to both$(Q,0)$ and $(0,Q)$ charge density wave order parameters occurring simultaneously in the same domain. Such a state could preserve C_4 symmetry, as in "checkerboard order" or, as in the proposed "criss-cross stripe" phase of Ref. 40, could break this and other point-group symmetries. This is to be contrasted with unidirectional or stripe order where a single wave vector CDW occurs per domain which necessarily implies breaking of C_4 rotational symmetry.[60]
[65] More complex states in which CDW order coexists with other orders, including an incommensurate dDW[35,47] and a CDW in a FL* phase[61,62], have been proposed which may offer a way to reconcile these observations.
[66] While the Yamaji angle is not experimentally observed close to its expected value $\theta = 59^\circ$, we note that if the unit cell were to be somehow doubled in the c-axis direction, a Yamaji angle would be possible near to 38°, which is exactly where an enhancement is observed. Because there is no compelling evidence for c-axis unit cell doubling, we ignore such a possibility in this work. Instead, the 'beat' near to 40° in our numerical analysis arises because of spin-zeros of the satellite peaks.
[67] We note that recent X-ray diffraction experiments in pulsed magnetic fields up to $30T$ have observed coherent (long ranged) charge density wave order which *does not* double the unit cell in the c direction
[68] While ARPES studies provide a direct measure of the electronic spectral function, and are therefore sensitive to the exact quasiparticle residue Z, this is not the same parameter which enters into the effective Fermi liquid parameter $t_\perp = \tilde{Z} t_\perp^{(0)}$ in QO experiments. Here, $\tilde{Z}$ is a measure of interlayer coherence, which in the limit of degenerate inter-layer perturbation theory becomes exactly the quasiparticle residue.[54]
[69] The γ_2 orbits involve tunneling from one layer to the next, and do not contribute in the limit of $t_\perp = 0$.
[70] In order to smoothen the Fourier transform, we have added another 2^{14} zeros to the ends of the data, and also employed a Kaiser window function with width parameter $\alpha = 2$ to eliminate ringing effects. We emphasize that this procedure introduces no additional harmonic content to the data.
[71] We note that such broken mirror symmetries may be detected by probing higher rank tensorial response functions in transport experiments.[63]
[72] Nevertheless, this is a breakdown orbit of the 'true' bonding and anti-bonding Fermi surfaces of the bilayer.
[73] QOs are suppressed by a factor of $e^{-B_D/B}$ where the Dingle reduction factor B_D can be written in terms of only the momentum-space circumference of the Fermi surface C_F and the mean-free path l_{free}, via $B_D = \hbar C_F / 2e l_{free}$.

Appendix A: Form of the Hamiltonian for general angles ϕ

For additional azimuthal angles as $\tan\phi = 1/M$ where $M \in \mathbb{Z}$ (or equivalently $\tan\phi = M$ by symmetry):

$$\vec{B} = B\left(\hat{z}\cos\theta + \hat{x}\sin\theta M/\sqrt{M^2+1} + \hat{y}\sin\theta/\sqrt{M^2+1}\right) \tag{A1}$$

we can no longer keep the translation symmetry along the $\hat{y}$ direction for arbitrary B with the chosen Landau gauge, however, we can define the new magnetic unit cell with the new lattice vectors $\hat{x}' = \hat{x}$, and $\hat{y}' = M\hat{x} + \hat{y}$ along $\vec{B}$ in plane or equivalently $x' = x - My$, $y' = y$. Once again we can choose a proper gauge so that the translation symmetry along the $\hat{y}'$ direction is preserved:

$$\begin{aligned}\boldsymbol{A} &= \left(0, 2\pi\Phi(x - My), -2\pi\Phi a_c \tan\theta (x - My)/\sqrt{M^2+1}\tan\theta\right) \\ &= \left(0, 2\pi\Phi x', -2\pi\Phi x' a_c \tan\theta/\sqrt{M^2+1}\right)\end{aligned} \tag{A2}$$

where $\Phi = B\cos\theta$ is the magnetic flux through the plaquette in the $x-y$ plane, and $\Phi a_c \tan\theta/\sqrt{M^2+1}$ is the flux through the $x-z$ plaquette. The hopping matrix elements no longer depend on y', therefore we can Fourier transform into the corresponding k'_y momentum basis. The resulting Hamiltonian (for each k'_y and spin σ) becomes:

$$\begin{aligned}\hat{H}_{k'_y,\sigma} &= \sum_{x,\lambda} t_{x,\lambda}\left[c^\dagger_{x+1,\lambda}c_{x,\lambda} + \text{H.c.}\right] + \frac{4\pi\tilde{g}\Phi\sigma}{\cos\theta}c^\dagger_{x,\lambda}c_{x,\lambda} \\ &+ \sum_{x,\lambda} t_{y,\lambda}\left[c^\dagger_{x-M,\lambda}c_{x,\lambda}\exp\left(i2\pi\Phi x - k'_y\right) + \text{H.c.}\right] \\ &+ \sum_{x} t_\perp\left[c^\dagger_{x,2}c_{x,1}\exp\left(i2\pi\Phi x a_c\tan\theta/\sqrt{M^2+1}\right) + \text{H.c.}\right]\end{aligned} \tag{A3}$$

where we have suppressed the k'_y and σ labels in the fermion operators. The Hamiltonian is still block tri-diagonal and its physical properties including DOS can be efficiently calculated using recursive Green's function method.

Appendix B: Mirror symmetry and the absence of breakdown frequencies

Here we discuss in further detail the absence of magnetic breakdown when a mirror symmetry relating the two planes of the bilayer is present. The essence of this symmetry argument is the following: in the presence of a magnetic field semiclassical dynamics correctly captures the motion of electrons, while magnetic breakdown is allowed as long as there exist matrix elements that take electrons from one orbit to the next. However, if there is a mirror plane perpendicular to the magnetic field, the mirror parity of the states remains a good quantum number even in the presence of a magnetic field. There are necessarily no matrix elements between states with different quantum numbers, and so breakdown processes are forbidden by this symmetry. We emphasize that this argument is also applicable in the limit of a single bilayer, i.e. when k_z is not a good quantum number.

This symmetry may be viewed at a more operational level by considering the Hamiltonian of a bilayer with identical dispersions $\varepsilon(\boldsymbol{k})$ in each layer. In the absence of a field, this takes the form

$$H = \sum_{\boldsymbol{k}} \Psi_{\boldsymbol{k}}\hat{H}_{\boldsymbol{k}}\Psi_{\boldsymbol{k}} = \sum_{\boldsymbol{k}=k_x,k_y}\begin{pmatrix}c^\dagger_{\boldsymbol{k},1} & c^\dagger_{\boldsymbol{k},2}\end{pmatrix}\begin{pmatrix}\varepsilon(\boldsymbol{k}) & t_\perp(\boldsymbol{k}) \\ t_\perp(\boldsymbol{k}) & \varepsilon(\boldsymbol{k})\end{pmatrix}\begin{pmatrix}c_{\boldsymbol{k},1} \\ c_{\boldsymbol{k},2}\end{pmatrix} \tag{B1}$$

where $t_\perp(\boldsymbol{k})$ is the (in general) momentum dependent tunneling between layers.

Mirror symmetry relating the two layers of the bilayer is akin to the statement that the Hamiltonian commutes with the x-Pauli matrix, $\hat{\tau}_x$:

$$\left[\hat{H}_{\boldsymbol{k}}, \hat{\tau}_x\right] = 0, \qquad \text{where } \hat{\tau}_x = \begin{pmatrix}0 & 1 \\ 1 & 0\end{pmatrix} \tag{B2}$$

It should be clear that this operation swaps the two planes of the bilayer, and so implements that mirror operation that we are referring to. The addition of a magnetic field $\boldsymbol{B}$ is typically implemented via a Peierls substitution, resulting in a dramatic change to the structure of the Hamiltonian and eigenstates. In particular, working in Landau gauge we only preserve translation invariance in a single direction, so in general the eigenstates will be labeled by a generalized Landau level index, n, and transverse momentum, k_y. However, as long as the magnetic field does not break this mirror symmetry, i.e. $\boldsymbol{B} = B_z\hat{z}$, it remains the case that eigenstates of $\hat{H}$ are also eigenstates of $\hat{\tau}_x$, i.e.

$$[\hat{H}, \hat{\tau}_x] = 0 \tag{B3}$$

$$\hat{H}|n, k_y, \pm\rangle = E_{(n,k_y,\pm)}|n, k_y, \pm\rangle \tag{B4}$$

$$\hat{\tau}_x|n, k_y, \pm\rangle = \pm|n, k_y, \pm\rangle \tag{B5}$$

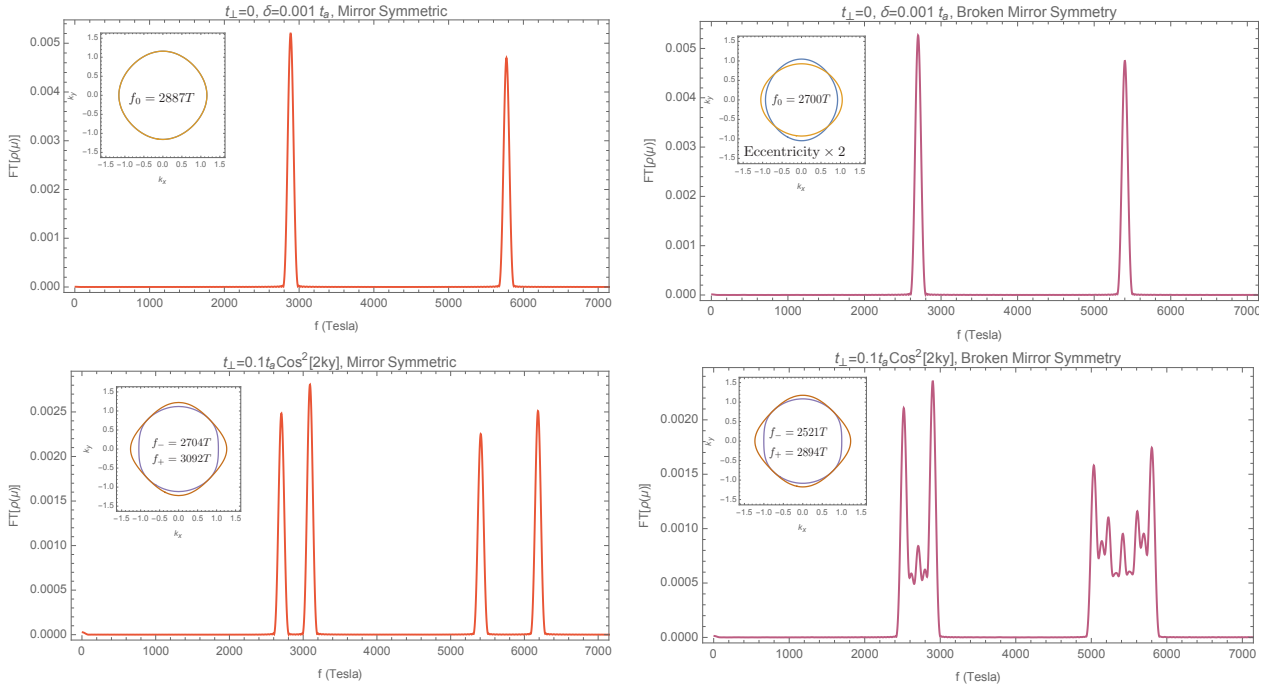

(a)Mirror symmetric (b)Broken mirror symmetry

FIG. 11: Fourier transforms of QOs in the density of states for two models (a) with mirror symmetry and (b) without mirror symmetry. In (a) we consider identical Fermi surfaces with an interlayer tunneling of the form $t_\perp(\boldsymbol{k}) = t_\perp \cos^2(2k_y)$, while in (b) the mirror symmetry is weakly broken by considering orthogonal Fermi surfaces with a weak mass anisotropy ($t_b = 0.95t_a$) and the interlayer tunneling has the same form as before. The bilayer bonding and anti bonding Fermi surfaces are almost identical in both cases, yet the QO frequencies are dramatically different: mirror symmetry forbids breakdown orbits in (a).

Note that these are the exact eigenstates of the system, and they are necessarily orthogonal. Also notice that none of these statements depend on the form of the interlayer tunneling $t_\perp(\boldsymbol{k})$.

The absence of magnetic breakdown is then most easily understood by considering the structure of the energy spectrum. Oscillations in any physical quantity arise because of periodicity in the structure of the energy spectrum as a function of $1/B$. The discrete two-fold mirror symmetry means that the Hamiltonian separates into two independent blocks, so that the energy spectrum for these $+$ and $-$ sectors can be solved independently. Because these sectors can be treated as independent systems, as the magnetic field is varied, each sector produces a **single** fundamental frequency in quantum oscillations. This results in two (possibly degenerate) quantum oscillation frequencies, with neither magnetic breakdowns nor beat (sum or difference) frequencies.

Fig. 11(a) and 11(b) provide confirmation of these symmetry arguments. In Fig. 11(a) we have considered identical dispersions $\varepsilon(\boldsymbol{k}) = -2t(\cos k_x + \cos k_y) - \mu$ with $t = 1$ and $\mu = -2.8t$, and $t_\perp(\boldsymbol{k}) = -0.1t\cos^2(2k_y)$. This form of the interlayer tunneling is both technically simple to implement, and produces nodes in the bilayer splitting. As is clear from the Fourier transform, no magnetic breakdown is present, and only two fundamental frequencies are seen when the interlayer tunneling is present. In Fig. 11(b) we weakly break the symmetry by considering dispersions of the form $\varepsilon(\boldsymbol{k}) = -2(t_a \cos k_x + t_b \cos k_y) - \mu$ in one layer, and $\varepsilon(\boldsymbol{k}) = -2(t_b \cos k_x + t_a \cos k_y) - \mu$ in the next layer, with $t_b = 0.95t_a$. In the absence of interlayer tunneling, only one frequency is seen in QOs (these pockets have identical areas), but a finite interlayer tunneling leads to multiple breakdown orbits.

Appendix C: Recursive Green's function method for the DOS of a tri-diagonal block Hamiltonian

As is shown in the main text, the Hamiltonian in k_y and σ basis only involves finite-range coupling and is block tri-diagonal

$$\hat{H}_{k_y,\sigma} = \begin{pmatrix} \ddots & \vdots & & & \\ \cdots & \hat{h}_{x-1,\sigma} & \hat{t} & & \\ & \hat{t} & \hat{h}_{x,\sigma} & \hat{t} & \\ & & \hat{t} & \hat{h}_{x+1,\sigma} & \cdots \\ & & & \vdots & \ddots \end{pmatrix}, \tag{C1}$$

$$\hat{h}_{x,\sigma} = \begin{pmatrix} 2t_{y,1}\cos(2\pi\Phi x - k_y) + \frac{4\pi\tilde{g}B\sigma}{\cos\theta} & t_\perp \exp(i2\pi\Phi a_c x\tan\theta) \\ t_\perp \exp(-i2\pi\Phi a_c x\tan\theta) & 2t_{y,2}\cos(2\pi\Phi x - k_y) + \frac{4\pi\tilde{g}B\sigma}{\cos\theta} \end{pmatrix}, \tag{C2}$$

$$\hat{t} = \begin{pmatrix} t_{x,1} & 0 \\ 0 & t_{x,2} \end{pmatrix} \tag{C3}$$

We are interested in the DOS $\rho_\sigma(\mu)$ of spin σ electrons at chemical potential μ defined as

$$\rho_\sigma(\mu) = -\frac{1}{\pi L_x}\mathrm{Tr}\left(\mathrm{Im}[\hat{G}_\sigma(\mu)]\right) \tag{C4}$$

$$\hat{G}_\sigma(\mu) = \left[(\mu + i\delta)\mathbb{I} - \hat{H}_{k_y,\sigma}\right]^{-1} \tag{C5}$$

where we have used the fact that the physical quantities are independent of k_y in the thermodynamic limit to suppress the summation over the k_y index.

To obtain the diagonal elements of the Green's function $\hat{G}_\sigma(\mu)$, we note the inverse of the following block tri-diagonal matrix may be calculated recursively

$$\hat{G}_\sigma^{-1}(\mu) = (\mu + i\delta)\mathbb{I} - \hat{H}_{k_y,\sigma} = \begin{pmatrix} \boldsymbol{a}_{1,1} & \boldsymbol{a}_{1,2} & & & \\ \boldsymbol{a}_{2,1} & \boldsymbol{a}_{2,2} & \boldsymbol{a}_{2,3} & & \\ & \boldsymbol{a}_{3,2} & \boldsymbol{a}_{3,3} & \boldsymbol{a}_{3,4} & \\ & & \ddots & \ddots & \ddots \end{pmatrix} \tag{C6}$$

where $\boldsymbol{a}_{i,i} = (\mu + i\delta)\mathbb{I} - \hat{h}_{x,\sigma}$ and $\boldsymbol{a}_{i,i+1} = \boldsymbol{a}_{i,i+1} = \hat{t}$. This is accomplished by the following recursive algorithm, which consists of two independent sweeps (and hence the computation is linear in the size L_x):

For increasing $i = 1, 2, \ldots, N-1$ we define

$$\boldsymbol{c}_i^L = -\boldsymbol{a}_{i+1,i}(\boldsymbol{d}_i^L)^{-1}, \tag{C7}$$

with $\boldsymbol{d}_1^L = \boldsymbol{a}_{1,1}$ and $\boldsymbol{d}_i^L = \boldsymbol{a}_{i,i} + \boldsymbol{c}_{i-1}^L\boldsymbol{a}_{i-1,i}$; for decreasing $i = N, N-1, \ldots, 2$ we define

$$\boldsymbol{c}_i^R = -\boldsymbol{a}_{i-1,i}(\boldsymbol{d}_i^R)^{-1}, \tag{C8}$$

where $\boldsymbol{d}_N^R = \boldsymbol{a}_{N,N}$ and $\boldsymbol{d}_i^R = \boldsymbol{a}_{i,i} + \boldsymbol{c}_{i+1}^R\boldsymbol{a}_{i+1,i}$, then the diagonal blocks of $\hat{G}_\sigma(\mu) = \left[(\mu + i\delta)\mathbb{I} - \hat{H}_{k_y,\sigma}\right]^{-1}$ are given by

$$\hat{G}_{i,i} = (-\boldsymbol{a}_{i,i} + \boldsymbol{d}_i^L + \boldsymbol{d}_i^R)^{-1}, \quad i = 1, 2, 3, \ldots, N \tag{C9}$$

Appendix D: Effective masses of electron pockets and Zeeman splitting coefficient $\tilde{g}$

1. Value of $\tilde{g}$ coefficient for Zeeman splitting in our tight-binding model

The effective mass of a band structure is defined as

$$m^* = \frac{\hbar^2}{2\pi}\frac{\partial S_k}{\partial \mu} \tag{D1}$$

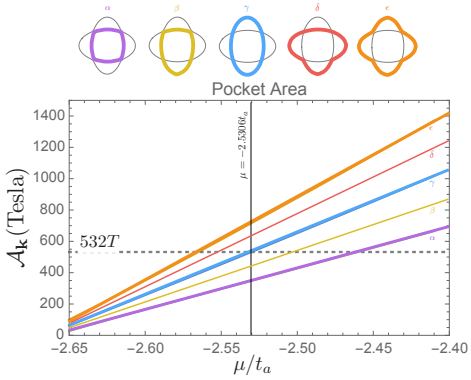

FIG. 12: Different slopes of S_k versus μ suggest the effective masses are different for the different orbits. The areas of α, γ and ϵ orbits are obtained from exact calculations of the Fermi surface, while for β and δ orbits the areas are based on interpolation between the α, γ and ϵ orbits (shown as the thinner lines). The vertical line is the value of $\mu = -2.5306t_a$ chosen throughout our calculations.

where S_k is the k-space area enclosed by the Fermi surface at chemical potential μ.

The dispersion relation in our tight-binding model in one of the single layers is equivalent to the 3rd orbit in Fig. 3

$$\epsilon_k = -2t_a \cos k_x a - 2t_b \cos k_y b \simeq -2t_a - 2t_b + t_a k_x^2 a^2 + t_b k_y^2 b^2 \tag{D2}$$

near the bottom of the band, where a and b are the sizes of the unit cell. At chemical potential μ the Fermi surface is close to an ellipsis with $k_x^0 = \sqrt{\frac{\mu}{t_a a^2}}$ and $k_y^0 = \sqrt{\frac{\mu}{t_b b^2}}$, thus the area enclosed by the Fermi surface

$$S_k = \pi k_x^0 k_y^0 = \frac{\pi\mu}{ab\sqrt{t_a t_b}} \tag{D3}$$

The effective mass of the model near the band bottom is

$$m^* = \frac{\hbar^2}{2ab\sqrt{t_a t_b}} \tag{D4}$$

By definition, the Zeeman splitting is

$$E_{Zeeman} = \pm\frac{g}{2}\mu_B B = \pm\frac{g\pi\hbar^2}{2abm_e}\frac{\Phi}{\cos\theta} = \pm\pi\sqrt{t_a t_b}\frac{gm^*}{m_e}\frac{\Phi}{\cos\theta} \tag{D5}$$

where $\mu_B = e\hbar/2m_e$ is the Bohr magneton and Φ is the dimensionless quantity of the number of magnetic flux quanta $\Phi_0 = h/e$ per $x-y$ plaquette.

Note that $g = 2$ for electron spin and $m^*/m_e \approx 1.6$ in YBCO, $t_a = 1$ and $t_b = 1/3$,

$$E_{Zeeman} \simeq \pm 0.92 \times 2\pi\Phi/\cos\theta \tag{D6}$$

In fact, the quadratic approximation in ϵ_k in Eq. D2 underestimates the effective mass m^* due to the higher order terms we have neglected. A more careful treatment and comparison between the numerical and theoretical θ dependence suggests the best choice is

$$E_{Zeeman} \simeq \pm 0.87 \times 2\pi\Phi/\cos\theta \tag{D7}$$

suggesting $\tilde{g} = 0.87$ in connection with Eq. 5.

2. Effective mass for different semiclassical orbits

While $\tilde{g} = 0.87$ determines the effective mass of the electron pocket in a single layer and the central peak in the QO power spectrum, it is conceivable that the effective mass of the other viable semiclassical cyclotron orbits associated with the side peaks be different, as their enclosed areas are necessarily modified. Fig. 12 shows the enclosed areas of these orbits as the chemical potential is varied, and the effective mass extracted from the corresponding slope according to Eq. D1. This is fully consistent with that obtained from the fit to QO amplitude versus θ angle of the magnetic field $\vec{B}$ in Fig. 6.

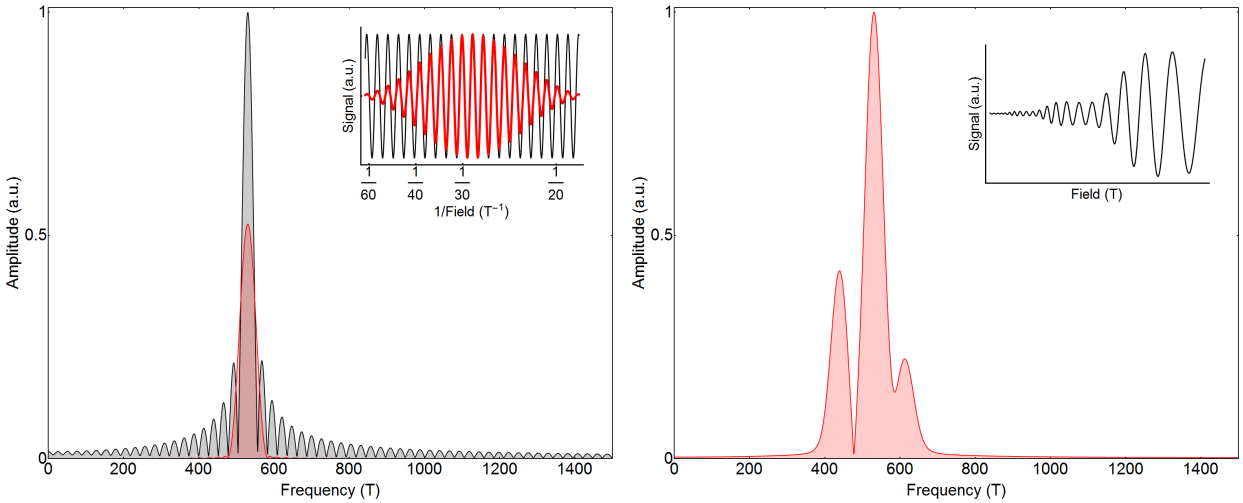

FIG. 13: **(a)** The inset shows two simulated data sets: one is apodized with a boxcar function (black), and the other uses equation E1 with $\alpha = 1.7$ (red). The Fourier transform of the boxcar-apodized data shows multiple side-lobes introduced from the sharp cut-off. The data apodized with the Kaiser window has a main peak suppressed by about a factor of two, but with the first side-lobe suppressed 20 times more than that in the box-car data. **(b)** The inset shows simulated data from equation E2 before the window is applied. The Fourier transform uses the Kaiser window with $\alpha = 1.7$—the same as the red curve in Fig. 13(a) and in Fig. 10 in the main text. Note that there are no extraneous side-lobes.

Appendix E: Fourier Transform Analysis

Fourier transforms of finite data sets are known to introduce frequency 'artifacts' into power-spectrum plots. These artifacts originate in the choice of how the data is truncated. For example, a 'boxcar' function—whereby the signal is simply truncated at the start and end—introduces high-frequency components due to the sharp cutoffs at the data boundaries. Modern signal processing solves this through 'apodization', whereby the data is brought to zero in some way at the boundary. The choice of apodization function depends on what features in the data are of interest.

The data in Fig. 10 were processed using a Kaiser window, designed to resolve closely-spaced frequencies while suppressing side-lobes (at the expense of absolute amplitude determination, which was not important for this analysis). The weighting function w for N data points is defined as

$$w(n) = \frac{I_0\left(\pi\alpha\sqrt{1-\left(\frac{2n}{N-1}-1\right)^2}\right)}{I_0(\pi\alpha)}, \tag{E1}$$

where I_0 is the zeroth modified Bessel function of the first kind and α controls the roll-off of the weighting function (chosen to be 1.7 for this work). Fig. 13(a) shows the effect of such a windowing function on a signal and its Fourier transform.

Simulated QO data is shown in the inset of Fig. 13(b). The data contains only the three central frequencies: 440, 530, and 620 T. Specifically, the function is

$$\tau = e^{-150/B}\left(\cos\left(\frac{2\pi\ 440}{B}-\pi\right)+\cos\left(\frac{2\pi\ 530}{B}-\pi\right)+\cos\left(\frac{2\pi\ 620}{B}-\pi\right)\right). \tag{E2}$$

Note the lack of side-lobes near 350 and 710 T: this demonstrates that the α and ϵ peaks in Fig. 10 are not artifacts of the data analysis.